

The Effects of the Spatial Distribution of Direct Anthropogenic Aerosols Radiative Forcing on Atmospheric Circulation

REI CHEMKE

Department of Applied Physics and Applied Mathematics, Columbia University, New York, New York

GUY DAGAN

Department of Earth and Planetary Sciences, Weizmann Institute of Science, Rehovot, Israel

(Manuscript received 15 October 2017, in final form 29 May 2018)

ABSTRACT

The large uncertainty in estimating the global aerosol radiative forcing (ARF) is one of the major challenges the climate community faces for climate projection. While the global-mean ARF may affect global quantities such as surface temperature, its spatial distribution may result in local thermodynamical and, thus, dynamical changes. Future changes in aerosol emissions distribution could further modulate the atmospheric circulation. Here, the effects of the spatial distribution of the direct anthropogenic ARF are studied using an idealized global circulation model, forced by a range of estimated-ARF amplitudes, based on the Copernicus Atmosphere Monitoring Service data. The spatial distribution of the estimated-ARF is globally decomposed, and the effects of the different modes on the circulation are studied. The most dominant spatial distribution feature is the cooling of the Northern Hemisphere in comparison to the Southern Hemisphere. This induces a negative meridional temperature gradient around the equator, which modulates the mean fields in the tropics. The ITCZ weakens and shifts southward, and the Northern (Southern) Hemisphere Hadley cell strengthens (weakens). The localization of the ARF in the Northern Hemisphere midlatitudes shifts the subtropical jet poleward and strengthens both the eddy-driven jet and Ferrel cell, because of the weakening of high-latitude eddy fluxes. Finally, the larger aerosol concentration in Asia compared to North America results in an equatorial superrotating jet. Understanding the effects of the different modes on the general circulation may help elucidate the circulation's future response to the projected changes in ARF distribution.

1. Introduction

Aerosols play a major role in the atmosphere's radiative balance. They directly interact with radiation and act to cool the atmosphere and surface by scattering the solar radiation (i.e., increasing albedo, mostly by sulfate and dust aerosols) and to warm the atmosphere by absorbing it (mostly through black carbon aerosols) (Ramanathan et al. 2001). In addition, aerosols have indirect radiative effects through their interactions with clouds. Increasing aerosol concentration increases the clouds' albedo (per given liquid water content) by enhancing the amount of water droplets (Twomey 1977). This was also suggested to result in warm rain suppression that may increase the clouds' lifetime (Albrecht 1989). The overall global mean anthropogenic aerosol radiative forcing (ARF), according to the last Intergovernmental

Panel on Climate Change (IPCC), is negative, but with large uncertainties that could even cancel this effect (Alexander et al. 2013).

Aerosols not only affect the global-mean temperature, but also modulate the horizontal and vertical temperature gradients as a result of their nonhomogeneous spatial and temporal distributions. As temperature gradients drive the atmospheric circulation both in the tropics (e.g., Held and Hou 1980; Held 2000) and in the extratropics, through baroclinic instability (e.g., Eady 1949; Pedlosky 1987), changes in aerosol loading may modulate the large-scale circulation in the atmosphere. Thus, studying the effects of the geographical distribution of aerosols on the dynamic and thermodynamic properties of the atmosphere is a key ingredient for understanding the atmospheric behavior in both present and projected climates.

For example, because most of the landmasses are in the Northern Hemisphere, which is also where most of

Corresponding author: Rei Chemke, rc3101@columbia.edu

the anthropogenic activity occurs, larger emissions of both natural and anthropogenic aerosols occur in the Northern Hemisphere compared to the Southern Hemisphere. The aerosols' net cooling effect results in a negative meridional temperature gradient around the equator, which may explain the southward shift of the intertropical convergence zone (ITCZ) in recent decades (e.g., Rotstayn et al. 2000; Williams et al. 2001; Rotstayn and Lohmann 2002; Ming and Ramaswamy 2009; Ming et al. 2011; Ming and Ramaswamy 2011; Hwang et al. 2013; Haywood et al. 2013; Ridley et al. 2015; Wang 2015; Allen et al. 2015; Voigt et al. 2017; Chung and Soden 2017). Furthermore, in global circulation models (GCMs), these temperature modulations were found to intensify the ascending branch of the clockwise (northern) Hadley circulation, resulting in a northward cross-equatorial energy flux (e.g., Ramaswamy and Chen 1997; Broccoli et al. 2006).

Because the anthropogenic aerosols' negative radiative forcing acts to weaken the positive forcing of greenhouse gases, the projected reduction in aerosols emissions together with the increase in greenhouse gas concentrations was argued to result in a northward shift of the ITCZ (e.g., Frierson and Hwang 2012; Allen 2015) and an overall widening of the Northern Hemisphere tropical circulation (Allen and Ajoku 2016).

Deeper investigation of the aerosols' effect on the ITCZ location revealed that black carbon aerosol loading results in a northward shift of the ITCZ and the Hadley cell edge (Allen et al. 2012a) by absorbing solar radiation, and thus warming the Northern Hemisphere more than the Southern Hemisphere (e.g., Roberts and Jones 2004; Wang 2004; Chung and Seinfeld 2005; Wang 2007; Yoshimori and Broccoli 2008; Allen and Sherwood 2011). Furthermore, the vertical location of black carbon absorption also affects the response of the circulation (e.g., Ban-Weiss et al. 2012) and was found to affect the direction of the ITCZ shift (Kim et al. 2015). Sulfate aerosols, on the other hand, cool the Northern Hemisphere more than the Southern Hemisphere by reflecting the incoming solar radiation, thus pushing the ITCZ southward (Yoshimori and Broccoli 2008). The aerosol-induced southward shift of the ITCZ is explained both by the direct effect of aerosol on the radiative balance and by the cooling of the Northern Hemisphere through the aerosols' interactions with clouds (Rotstayn et al. 2000; Rotstayn and Lohmann 2002; Williams et al. 2001; Chung and Soden 2017).

Aerosols not only affect the Hadley circulation through radiative processes, but their interactions with clouds may also alter the thermodynamic properties of the atmosphere by modulating the moisture content (Dagan et al. 2016, 2017) and affecting the strength of

the tropical hydrological cycle (Dagan and Chemke 2016). Enhanced aerosol loading suppresses precipitation in subtropical warm convective clouds (Albrecht 1989), which was shown to enhance the equatorward moisture flux at the lower branch of the Hadley cell (the trade winds) in an idealized GCM. This strengthens the ITCZ and the entire Hadley circulation, which results in a further suppression of subtropical rain, and hence acts as a positive feedback for subtropical aerosol loading (Dagan and Chemke 2016).

Aerosols also modulate the atmospheric circulation in the extratropics. For example, Northern Hemisphere tropical volcanic eruptions were found to increase the polar vortex (strong westerlies). By increasing stratospheric sulfate aerosol concentrations, which absorb both solar and longwave radiation, tropical volcanic eruptions result in warming of the tropical stratosphere. This increases the stratospheric equator-to-pole temperature gradient, which enhances the winter polar vortex (e.g., Robock 2000; Shindell et al. 2004; Allen and Sherwood 2011).

At midlatitudes, increased aerosol loading was found to decrease the meridional energy flux (e.g., Ming et al. 2011; Ming and Ramaswamy 2011) and to strengthen the momentum flux convergence, which shifts the Northern Hemisphere extratropical jet poleward (Allen and Sherwood 2011). The latter is driven by the direct effect of anthropogenic aerosols.

In this study, an idealized GCM is used to study the effects of the spatial distribution of the direct anthropogenic ARF on the general circulation. While most previous studies investigated the effects of the global ARF on the general circulation (mostly in the tropics), here, by spatially decomposing the ARF, we study the dynamical and thermodynamical responses of the atmosphere to different spatial structures of the ARF. In projected scenarios, aerosol emissions are expected to decrease. However, the atmospheric circulation is sensitive to the spatial distribution of the aerosols. Thus, using the analysis of this paper, understating how the aerosols will be distributed in the future may help projecting the atmospheric circulation response.

Section 2 describes the idealized GCM and the decomposition method for the ARF that is used in this study. Sections 3–5 show the effects of the global, zonally symmetric, and zonally asymmetric ARF on the global circulation, respectively, and section 6 summarizes the results.

2. Methods

The Geophysical Fluid Dynamics Laboratory (GFDL) idealized aquaplanet GCM is coupled to a slab ocean,

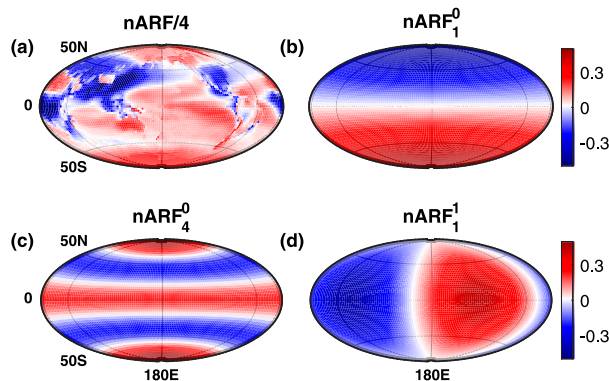


FIG. 1. The nARF as a function of latitude and longitude. (a) The full nARF from CAMS (2003–12; normalized such that its global-mean value is zero). The three most dominant modes of the ARF using spherical harmonics as basis function, with (b) nARF_1^0 , (c) nARF_4^0 , and (d) nARF_1^1 . These modes explain 20.3%, 10.3%, and 8.8% of the variance, respectively. For ease of comparison, the full nARF in (a) is divided by 4.

which exchanges heat (through sensible, latent, and radiative fluxes), momentum, and moisture with the atmosphere using the simplified Monin–Obukhov similarity theory (Frierson et al. 2006). The model is forced by latitudinal distributed solar radiation at the top of the atmosphere, which exponentially decays toward the surface. Radiative transfers are calculated using a two-stream gray radiation scheme with a parameterized optical depth that is a function of latitude and sigma (the vertical coordinate of the model, $\sigma = pp_s^{-1}$, is pressure normalized by surface pressure) (Goody and Yung 1995). The vertical structure of the optical depth is composed of two components that mimic the vertical structure of water vapor and well-mixed gases. Since the optical thickness is only a function of latitude and sigma, it does not account for any radiative feedbacks (changes in clouds, water vapor, etc.). At the surface, a constant planetary albedo of 0.36 reflects the solar radiation. The parameters in the radiation scheme are as described in Chemke (2017). The primitive equations are solved on a sphere with a spectral T42 horizontal resolution ($2.7^\circ \times 2.7^\circ$), 30 vertical sigma layers, and 6-h time resolution.

For studying the effects of the ARF's spatial distribution on the general circulation, the anthropogenic aerosols' direct shortwave forcing (Fig. 1a), from the Copernicus Atmosphere Monitoring Service (CAMS), is decomposed using spherical harmonics as basis functions (ARF_n^m , where n and m are the total and zonal wavenumbers, respectively; Figs. 1b–d). CAMS calculates the ARF using the aerosol properties from the Monitoring Atmospheric Composition and Climate (MACC) project (Inness et al. 2013). The MACC project provides aerosol reanalysis data that constrain models to observations of both ground-based stations (AERONET sites)

and the Moderate Resolution Imaging Spectroradiometer (MODIS) (e.g., Kinne et al. 2013). Using radiative transfer schemes (Mlawer et al. 1997; Key and Schweiger 1998; Stevens et al. 2013), CAMS produces daily anthropogenic aerosol radiative forcing between 2003 and 2012, as described in Bellouin et al. (2013). The direct anthropogenic ARF has a global-mean value at the top of the atmosphere of -0.7 W m^{-2} , which is within the reported range from -0.85 to 0.15 W m^{-2} in the last IPCC report (Alexander et al. 2013).

As mentioned in section 1, aerosols may modulate the temperature field by both changing its spatial structure and its global-mean value. A global change in temperature (even if driven by radiative forcing that is homogeneously distributed) would affect the global circulation (e.g., Held and Soden 2006; Vallis et al. 2015). To focus only on the effects of the spatial distribution of anthropogenic aerosols on the circulation, the ARF is normalized such that its global average value is 0. This is done by subtracting the global-mean value of the ARF and then dividing by it. Because we force the model with different normalized ARF (nARF) amplitudes (as discussed below), dividing by the global-mean ARF value sets the baseline amplitude of the nARF to follow the spatial ARF amplitude. The three most dominant modes (largest amplitudes) and the full nARF (Fig. 1) are used separately to force the temperature in the troposphere. Because this is a zonally symmetric aquaplanet model, any zonal asymmetries in these simulation arise only from the nARF forcing. Since we force only the atmosphere, and not the surface (see below), using the shortwave ARF (which does not account the cooling of the atmosphere resulting from the reduced upward surface longwave radiation and heat flux), we estimate the ARF prior to normalization to be the average of the top of the atmosphere and surface ARF. This allows us to account for both the aerosols' atmospheric warming effect through absorption of shortwave radiation and their dominant atmospheric cooling effect through changes in surface energy balance (i.e., less shortwave radiation is absorbed at the surface, which results in less heat flux and longwave radiation emitted from the surface to the atmosphere).

As discussed in section 1, the vertical location of the ARF may result in different thermodynamic and circulation changes (Ban-Weiss et al. 2012; Kim et al. 2015). Since here we wish to study only the effects of the horizontal distribution of aerosols on the circulation, we keep its vertical distribution as simple as possible. The nARF's vertical distribution is simplified by applying the nARF equally through all layers only in the troposphere. This represents the high concentrations of aerosols below the tropopause in comparison to that of the

stratosphere. Including a more realistic vertical distributions of aerosols would require decomposing the nARF at each level, which would result in different dominant modes for each level. We account here only the anthropogenic aerosols' direct effect from CAMS because their indirect effect is not available poleward of 60° latitude, which would result in biases toward symmetric zonal modes at high latitudes.

The model's temperature equation can be written as follows:

$$\frac{\partial T}{\partial t} = -\mathbf{u} \cdot \nabla T + Q_{\text{surf}} + Q_{\text{adiab}} + Q_{\text{moist}} + Q_{\text{rad}}, \quad (1)$$

where T is the temperature and \mathbf{u} is the horizontal velocity vector; Q_{surf} and Q_{adiab} are the heat exchange between the lower atmospheric level and the surface, and the adiabatic heating, respectively. Moist processes (Q_{moist} , latent heat release per unit mass) are parameterized using large-scale condensation and convection schemes. The former keeps the specific humidity below 100% via precipitating condensed water vapor, and the latter relaxes the temperature and humidity toward moist adiabatic profiles (Betts 1986; Betts and Miller 1986).

The diabatic radiation term Q_{rad} in Eq. (1), which accounts for longwave and solar radiation and nARF, is calculated as

$$Q_{\text{rad}} = \frac{1}{C_p} \frac{d(Q_s - Q_l + \alpha \text{nARF})}{dm}, \quad (2)$$

where dm (kg m^{-2}) is the atmospheric mass per unit area between two vertical layers, $C_p = 1004 \text{ J kg}^{-1} \text{ K}^{-1}$ is specific heat capacity of air, and Q_l and Q_s are the longwave and solar radiative fluxes (W m^{-2}), respectively. Here α is a parameter that varies between 0.5 and 10 W m^{-2} , which sets the amplitude of the nARF; $\alpha = 0 \text{ W m}^{-2}$ corresponds to the reference simulation where the nARF does not affect the temperature field (see section 3a) and the circulation is symmetric around the equator. The nARF, thus, does not affect the constant solar radiative flux, but is added on top of it. The nARF, however, may modulate the longwave radiative fluxes by changing the temperature field. Furthermore, as discussed above, cloud processes are represented by moist convection, large-scale condensation, and constant planetary albedo. Hence, changes in nARF do not interact with clouds through microphysical processes, but they may affect the temperature fields, and thus convection processes as well. Note that the surface (ocean slab) temperature equation is not forced by the nARF,

but only responds to changes in the lower-atmosphere temperature field. The results below represent the last 1000 days of 5000-day model run to ensure that a statistically steady state is reached.

The implications of using an idealized GCM with the above simplified vertical structure of nARF are discussed in section 6. While the above analysis could be done in a comprehensive GCM, its numerous internal feedbacks would only mask the relation we seek to understand between the ARF's spatial distribution and the atmospheric circulation. The relative simplicity of the idealized GCM (lacks land, chemical reaction, clouds, ice, etc.), on the other hand, allows us to study and isolate the dynamical response of the atmosphere to different amplitudes and structures of the ARF. As further discussed below, in spite of the model's idealization, it is able to capture circulation changes as in previous studies, which examined the effects of the total ARF in comprehensive GCMs. This gives us further confidence that the presented qualitative results are not sensitive to the idealistic nature of the model.

3. The ARF's effects on the general circulation

a. Reference simulation

The reference simulation ($\alpha = 0 \text{ W m}^{-2}$) represents Earth's present-day climate with mean surface temperature of 287 K and equator–pole temperature difference of 41 K. It is symmetric around the equator, and each hemisphere has a Hadley cell extending from the equator to approximately 23° latitude, and an extratropical Ferrel cell (Fig. 2a). In each hemisphere the subtropical and eddy-driven jets are partially merged, as the subtropical jet is at the edge of the Hadley cell at approximately 26° latitude and the eddy-driven jet is at midlatitudes around 40° (Fig. 2b). The latter resides in the Ferrel cell and is driven by the divergence of the Eliassen–Palm (EP) flux (Edmon et al. 1980, black arrows in Fig. 2b), where its meridional and vertical components are

$$-a \cos \varphi (\overline{u'v'}), \quad (3)$$

and

$$a \cos \varphi \left[f \overline{v'\theta} \left(\frac{\partial \theta}{\partial p} \right)^{-1} \right], \quad (4)$$

respectively. Here a is Earth's radius, φ is latitude, u and v are the zonal and meridional velocities, respectively, the prime denotes deviation from zonal mean (denoted by the overbar), f is the Coriolis parameter, and θ is potential temperature. The vertical component [Eq. (4)]

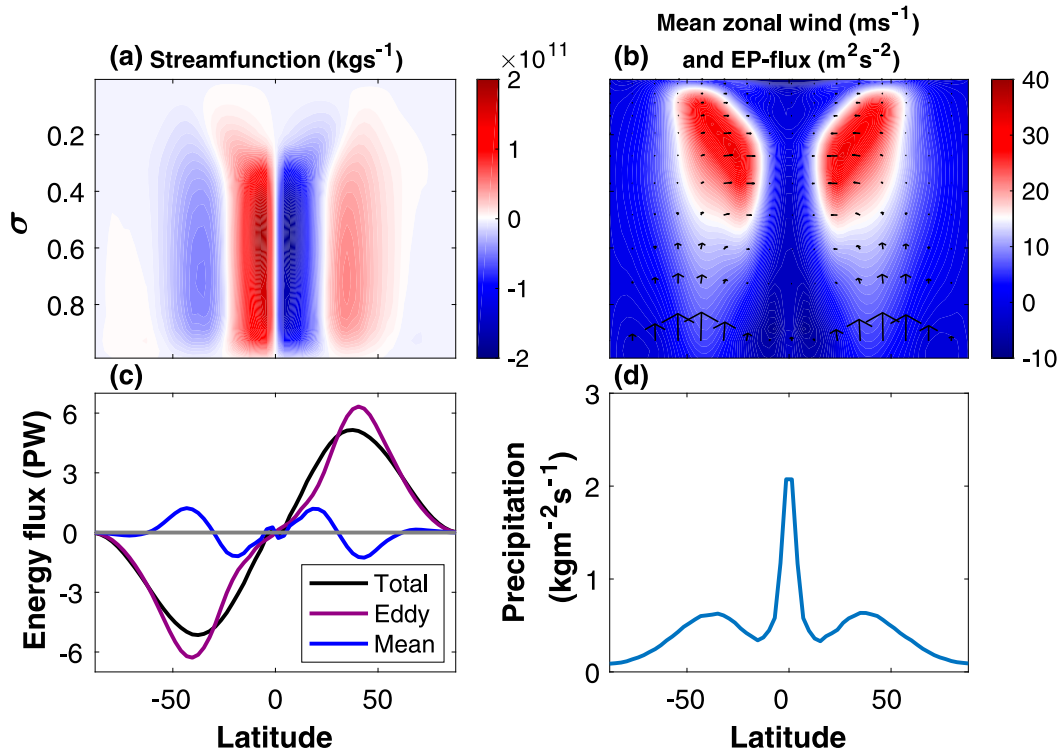


FIG. 2. Zonal and time mean fields from the reference simulation: (a) meridional mass streamfunction (kg s^{-1}); (b) zonal wind (m s^{-1} ; color shading) and EP flux ($\text{m}^2 \text{s}^{-2}$; vectors); (c) vertically integrated meridional flux of total (black), mean (blue), and eddy (purple) moist static energy (PW); and (d) precipitation ($10^{-4} \text{kg m}^{-2} \text{s}^{-1}$).

represents the meridional eddy heat fluxes, which arise from baroclinic instability (e.g., Eady 1949), and transfers energy upward. Aloft, the energy is deflected equatorward by the meridional component of the EP flux, which deposits momentum to the mean flow (the eddy driven jet). The Ferrel cell is driven by the meridional derivative of the eddy momentum and heat fluxes (Vallis 2006).

The dominance of eddies at midlatitudes is also demonstrated using the meridional moist static energy flux (Fig. 2c). While eddies are responsible for most of the energy transfer at midlatitudes, the mean flow contributes to the poleward flux at the Hadley cell. The reference simulation produces maximum precipitation at the equator (similar to the ITCZ; Fig. 2d), because of convection in the ascending branch of the Hadley cell, and a local minimum at the subtropics, where air descends.

b. The full ARF

For studying the ARF's effects on the general circulation, we first add the full nARF from CAMS (Fig. 1a) to the radiation heating term [Eq. (2)] in the temperature equation. By changing the nARF's magnitude (modifying the α parameter), we study the response of both the mean flow and eddy fields to the forcing. Later, we decompose the full nARF to better understand

which spatial structure is responsible for the observed circulation changes (see sections 4 and 5).

1) THE MEAN ZONAL FIELDS' RESPONSE TO ARF

Figure 3 shows the differences in the meridional mass streamfunction (color shading in Fig. 3a), mean zonal wind (color shading in Fig. 3b), EP flux (gray arrows in Fig. 3b), meridional moist static energy flux (Fig. 3c), and precipitation (Fig. 3d) between simulation with nARF and $\alpha = 1 \text{ W m}^{-2}$ and the reference simulation. Contours in Figs. 3a and 3b show the circulation from the reference simulation ($\alpha = 0 \text{ W m}^{-2}$).

The nARF acts to strengthen the Northern Hemisphere Hadley circulation (blue colors with dashed streamlines in Fig. 3a) and to weaken the Hadley circulation in the Southern Hemisphere (blue colors with solid streamlines in Fig. 3a), as was found in previous studies (e.g., Ramaswamy and Chen 1997; Broccoli et al. 2006; Ming and Ramaswamy 2011). Not only the tropical circulation strength changes, but also its location. The ITCZ shifts southward (as in Northern Hemisphere wintertime) (Fig. 3d), which results in a positive cross-equatorial moist energy flux (positive values of the black line at the equator in Fig. 3c). As the tropical circulation is mostly driven by the mean fields (Held and Hou

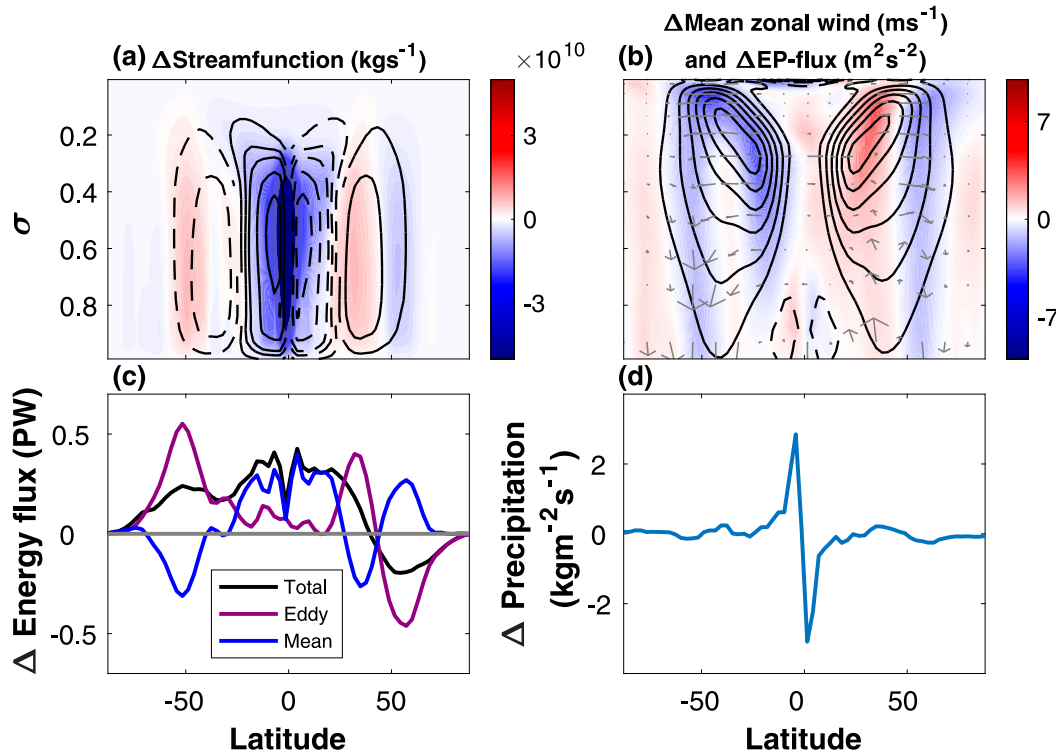


FIG. 3. Differences in zonal and time mean fields between simulation with full nARF, with $\alpha = 1 \text{ W m}^{-2}$, and the reference simulation (Fig. 2): (a) meridional mass streamfunction (kg s^{-1}); (b) zonal wind (m s^{-1} ; color shading) and EP flux ($\text{m}^2 \text{s}^{-2}$; vectors), (c) vertically integrated meridional flux of total (black), mean (blue), and eddy (purple) moist static energy (PW); and (d) precipitation ($10^{-5} \text{ kg m}^{-2} \text{s}^{-1}$). In (a) and (b) the black solid and dashed contours respectively represent positive and negative values from the reference simulation. Contours values in (a) are $\pm 0.1, \pm 0.3, \pm 0.5, \pm 1.0$, and $\pm 1.6 \times 10^{11} \text{ kg s}^{-1}$, and min and max contours in (b) correspond to -5 and 30 m s^{-1} , respectively, with a contour interval of 5 m s^{-1} .

1980), this cross-equatorial energy flux is mostly due to mean field changes. While the weakening of the tropical Southern Hemisphere's Hadley cell is accompanied with a weaker mean poleward energy flux, the strengthening of the Northern Hemisphere's Hadley cell is accompanied with a stronger mean poleward energy flux.

The nARF modulates not only the tropical but also the extratropical circulation. The Northern Hemisphere subtropical jet strengthens mostly at high altitudes, whereas its southern counterpart weakens (Fig. 3b). As further discussed below, the spatial distribution of the nARF (Fig. 1a) acts to strengthen the subtropical meridional temperature gradient in the Northern Hemisphere and to weaken it in the Southern Hemisphere. Following both Held and Hou (1980) and Lindzen and Hou (1988), an increase (decrease) in the meridional temperature gradient acts to strengthen (weaken) the Hadley cell circulation. The strengthening of the Northern Hemisphere Hadley circulation, which transfers more heat to its edge (Fig. 3c), results in a larger meridional temperature gradient at the subtropics. Based on thermal

wind balance, the larger meridional temperature gradient in the Northern Hemisphere is accompanied with stronger vertical shear of the zonal wind (Fig. 3b). The same arguments may explain the weaker vertical shear of the zonal wind in the Southern Hemisphere, where the Hadley circulation weakens.

At midlatitudes in the Southern Hemisphere, the EP flux weakens through all latitudes and altitudes (gray arrows in Fig. 3b). Changes of the EP flux are pointing poleward and downward, which are opposite to their reference state (black arrows Fig. 2b). As the EP flux decreases more in regions where it was larger (i.e., at low altitudes in midlatitudes and at high altitudes on the eddy-driven jet's equatorward flank), its divergence decreases, and concomitantly, both the Ferrel cell and the eddy-driven jet weaken and become narrower (Figs. 3a,b). A similar picture occurs in the Northern Hemisphere on the poleward flank of the eddy-driven jet. On the latter's equatorward flank, the lateral component of the EP flux decreases more in region where it was weaker, and its vertical component even strengthens

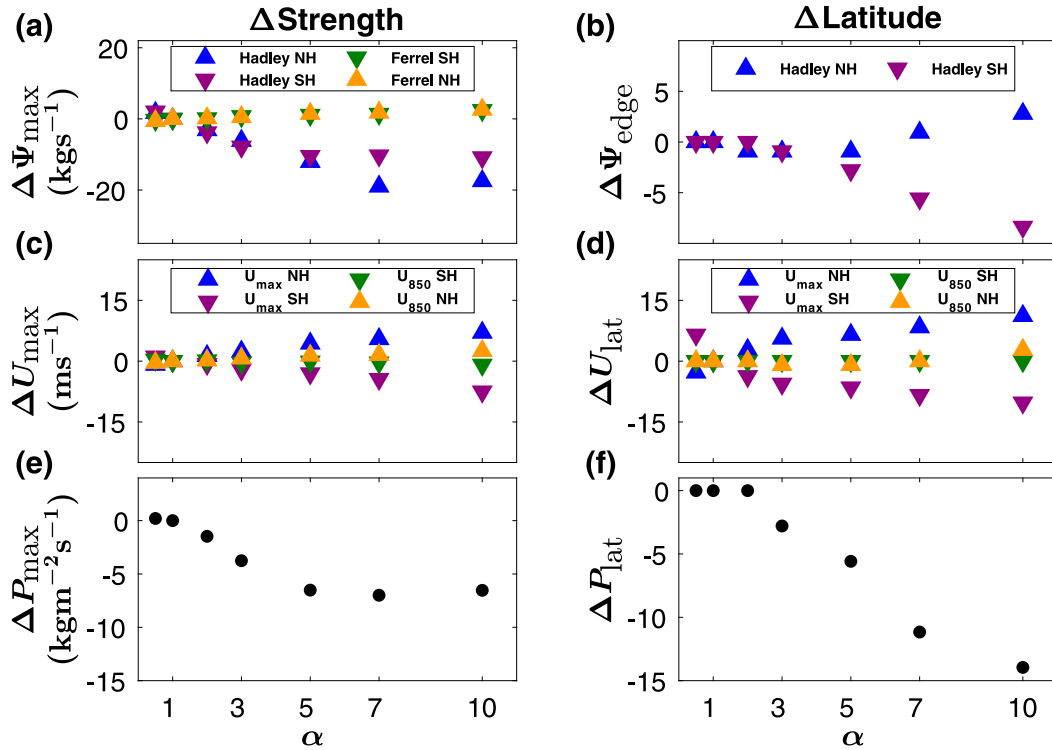


FIG. 4. The (a),(c),(e) strength and (b),(d),(f) latitudinal location of the mean fields from simulations with full nARF from CAMS (Fig. 1a) relative to a simulation with $\alpha = 1 \text{ W m}^{-2}$, as a function of α , which controls the amplitude of the aerosol forcing. In (a)–(d) upward (downward) triangles represent Northern (Southern) Hemisphere values. The Hadley (blue and purple triangles) and Ferrel (orange and green triangles) cells' strength ($10^{10} \text{ kg s}^{-1}$) are shown in (a). The Hadley cell edge (in latitude, defined where the meridional mass streamfunction first changes sign at the height of its max value) is shown in (b). The max zonal wind strength (blue and purple triangles) and zonal wind at 850 hPa (orange and green triangles) (m s^{-1}) are shown in (c). Latitude of max zonal wind (blue and purple triangles) and of eddy-driven jet (based on max zonal wind at 850 hPa; orange and green triangles) are shown in (d). (e),(f) Max precipitation intensity ($10^{-5} \text{ kg m}^{-2} \text{s}^{-1}$) and latitude, respectively.

(upward pointing gray arrows in Fig. 3b), resulting in a stronger Ferrel cell (Fig. 3a) and eddy-driven jet (red colors in the Northern Hemisphere in Fig. 3b).

This opposite tendency of the vertical component of the EP flux in the Northern Hemisphere to increase on the equatorward flank and decrease on the poleward flank of the eddy-driven jet can also be seen in the meridional eddy moist static energy flux (purple lines in Fig. 3c). In the Northern Hemisphere, the eddies transfer more (less) energy on the equatorward (poleward) flank of the Ferrel cell. In the Southern Hemisphere, the eddies transfer less energy poleward (positive values of the purple line), in concert with the weakening of the EP flux. Opposite results were reported in Allen and Sherwood (2011), who showed a northward shift of the ITCZ, weakening of the Northern Hemisphere tropical circulation, and weakening (strengthening) of the EP flux at middle (high) latitudes. The disagreement with Allen and Sherwood (2011) stems from the fact that in their simulations the anthropogenic ARF tended to warm the Northern Hemisphere, whereas here it tends to cool it.

For a deeper understanding of the ARF's effects on the general circulation, and for studying the circulation's response to different nARF's amplitudes, we vary the α parameter between 0.5 and 10 W m^{-2} , and plot the mean fields' response to different values of α (Fig. 4).

Increasing the nARF's amplitude results in a further strengthening of the Northern Hemisphere Hadley circulation (its clockwise circulation becomes more negative; upward pointing blue triangles in Fig. 4a) and in a further weakening of the southern Hadley circulation (its direct circulation becomes less positive; see the downward pointing purple triangles in Fig. 4a). At high nARF amplitudes ($\alpha > 7 \text{ W m}^{-2}$) both changes in circulation strength saturate. Interestingly, the weakening of the Southern Hemisphere circulation, rather than the strengthening of the Northern Hemisphere circulation, affects more the ascending branch at the ITCZ, since the precipitation intensity also weakens until saturation with nARF (Fig. 4e).

The latitudinal location of the ascending branch of the Hadley cell (the location of the ITCZ) further shifts southward with nARF, and unlike precipitation intensity, it does not saturate at high nARF (Fig. 4f). The latitudinal shift occurs mostly for the ascending branches of the Hadley cells, while the descending branches show minor poleward shifts only at high nARF amplitudes (Fig. 4b). Previous studies found that aerosols act to contract the tropical circulation, mostly via their indirect radiative effect (Allen and Ajoku 2016). This, together with the simplified nARF vertical distribution [cf. Ban-Weiss et al. (2012) and Kim et al. (2015) for a discussion on the effect of the vertical structure of the ARF on the circulation] might explain why in these simulations, which include only the direct radiative effect, no such contraction is observed.

As discussed above, the southward shift of the ITCZ together with the increase of the Northern Hemisphere Hadley circulation's strength results in a stronger cross-equatorial energy flux with nARF amplitude (Figs. 5a–c). In concert with the strengthening (weakening) of the Northern (Southern) Hemisphere tropical circulation with nARF, its mean meridional energy flux at the tropics strengthens (weakens) as well. Not only the mean flow is subjected to changes around the equator, but also the eddy fields. Figure 5d shows the tropospheric vertically averaged mean eddy momentum flux convergence (EMFC), $(-1/a \cos^2 \varphi)(\partial u'v' \cos^2 \varphi / \partial \varphi)$, for three nARF amplitudes. The EMFC increases with nARF both around the equator and around 15°S. This results in a super-rotation around the equator (westerlies) and a decrease in the Southern Hemisphere tropical easterlies, as can be seen in Fig. 3b.

The mean zonal wind has a monotonic response to increasing the nARF's amplitude. The Northern Hemisphere subtropical jet further strengthens (upward pointing blue triangles in Fig. 4c) while the southern jet further weakens (downward pointing purple triangles in Fig. 4c) with nARF. This occurs in both upper- and lower-level jets (orange and green triangles in Fig. 4c). The subtropical jets in both hemispheres shift poleward with nARF, resulting in a further merging and narrowing of the subtropical and eddy-driven jets (Fig. 4d). The eddy-driven jet, however, shows minor latitudinal variations with nARF (orange and green triangles in Fig. 4d). Concomitantly, the EMFC at midlatitudes increases in the Northern Hemisphere and decreases in the Southern Hemisphere (Fig. 5d). These changes in EMFC together with the decrease of the eddy moist static energy on the poleward flanks of the Ferrel cells in both hemispheres (purple lines in Figs. 5a–c) intensify the Ferrel cell in the Northern Hemisphere and weaken it in the Southern Hemisphere (orange and green triangles in Fig. 4a). This,

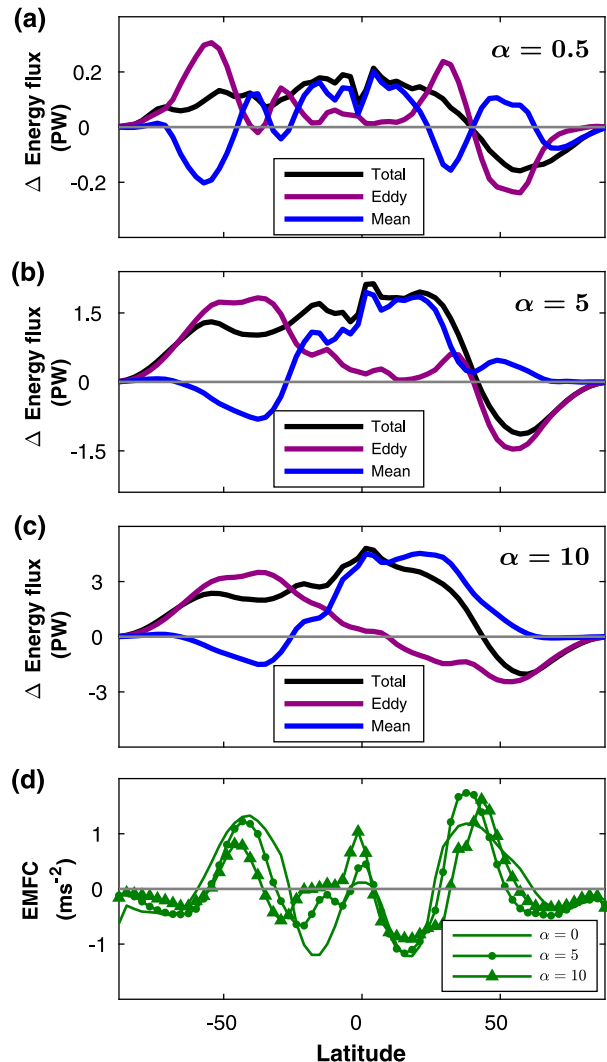


FIG. 5. Zonal and time mean eddy flow response to full nARF from CAMS (Fig. 1a) as a function of latitude. Note the different y axes in all panels. (a)–(c) As in Fig. 3c, but showing the differences in vertically integrated moist static energy flux (PW) between simulations with nARF using $\alpha = 0.5, 5$, and 10 W m^{-2} , respectively, and the reference simulation. Black, blue, and purple lines correspond to meridional flux of total, mean, and eddy moist static energy, respectively. (d) Tropospheric vertically averaged EMFC [10^{-5} m s^{-2} ; the meridional component of the divergence of the EP flux Eq. (3)] from the reference simulation (solid line), and simulations with full nARF using $\alpha = 5$ (circles) and 10 W m^{-2} (triangles).

as further discussed below, is different from the results of Ceppi et al. (2013), where extratropical Northern Hemisphere cooling resulted in a poleward shift of the Southern Hemisphere eddy-driven jet, mostly because here other forcings affect the jets beside the cooling in the Northern Hemisphere.

In summary, the nARF is found to intensify the Northern Hemisphere Hadley cell, weaken the Southern Hemisphere

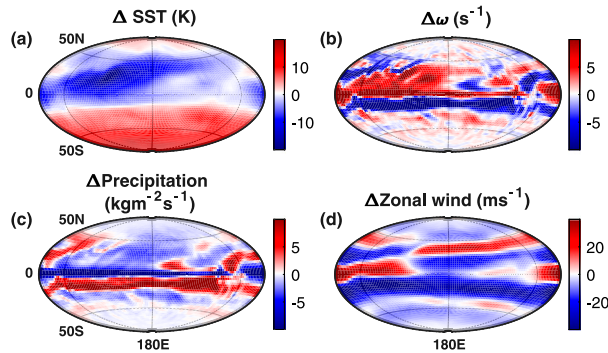


FIG. 6. Differences in time mean fields between simulation with full nARF, with $\alpha = 10 \text{ W m}^{-2}$, and the reference simulation: (a) surface temperature (K); (b) vertical wind (10^{-7} s^{-1}) at the level of its max value at the ITCZ (720 hPa), where positive (negative) values indicate descending (ascending); (c) precipitation ($10^{-5} \text{ kg m}^{-2} \text{ s}^{-1}$); and (d) zonal wind (ms^{-1}) at the level of its max equatorial value (320 hPa).

Hadley cell, and decrease the ITCZ's precipitation. While the latter shifts southward with nARF, resulting in a positive cross-equatorial energy flux, only a minor shift of the Hadley cells' edge is observed. The subtropical jet shifts poleward and further merges with the eddy-driven jet (which shows minor latitudinal changes) in both hemispheres, but while it strengthens in the Northern Hemisphere, it weakens in the Southern Hemisphere. The eddy momentum and energy fluxes overall weaken with nARF at midlatitudes. However, this weakening occurs more at middle-to-high latitudes than at low-to-middle latitudes, which increases their meridional gradient in the Northern Hemisphere and decreases it in the Southern Hemisphere. This is in concert with the strengthening of the Ferrel cell and eddy-driven jet in the Northern Hemisphere, and their weakening in the Southern Hemisphere.

2) THE ZONALLY ASYMMETRIC FIELDS' RESPONSE TO ARF

The zonal mean findings from the full nARF simulations, as well as the behavior of the zonally asymmetric time mean fields, are observed by plotting the differences in the mean fields between the full nARF simulation (Fig. 1a) with $\alpha = 10 \text{ W m}^{-2}$ and the reference simulation as a function of latitude and longitude (Fig. 6). As discussed above, the nARF acts to cool the Northern Hemisphere relative to the Southern Hemisphere (Fig. 6a) and push the ITCZ southward as can be seen by both the vertical velocity (Fig. 6b) and precipitation (Fig. 6c) fields. In addition, similar to Fig. 3b, the nARF increases the upper-level zonal wind (at the level of its maximum value) around the equator and in the Northern Hemisphere extratropics, while decreasing it in the Southern Hemisphere (Fig. 6d).

In addition to these hemispherical differences, in the Northern Hemisphere the nARF acts to cool eastern longitudes (45°E – 180°) more than western longitudes (180° – 45°W). In the subtropics, this zonal temperature gradient increases the meridional wind aloft (upper branch of the Hadley cell) caused by the thermal wind balance. From continuity, the descending air (the descending branch of the Hadley cell) at these longitudes (red colors in Fig. 6b) strengthens, as was shown in Ming and Ramaswamy (2011). These are in concert with weaker precipitation intensity in eastern longitudes in the Northern Hemisphere (Fig. 6c). The equatorial superrotating zonal wind is also localized only on half of the longitudes (Fig. 6d), and this point is further discussed later (section 5).

4. The zonally symmetric modes of the ARF

For a better understanding of the circulation's response to the ARF's geographical distribution (section 3), we separately force the model with the nARF's three most dominant modes, based on spherical harmonic decomposition (Figs. 1b–d).

a. ARF_1^0

The nARF's most dominant mode, which explains 20.3% of the variance, represents the tendency of the full nARF to cool the Northern Hemisphere relative to the Southern Hemisphere (Fig. 1b). This mode captures most of the mean fields' behavior, especially in the tropics, under different amplitudes of forcing (Fig. 7). Figure 7 shows the same fields as in Fig. 4 only for simulations forced by the mode with total wavenumber 1 and 0 for the zonal wavenumber (nARF_1^0 ; Fig. 1b). Lindzen and Hou (1988) showed that as the asymmetrical heating around the equator increases (e.g., in winter and summertime) the Hadley cell shifts off the equator and intensifies. Similar to their and Broccoli et al.'s (2006) results, the nARF_1^0 acts to strengthen the Northern Hemisphere Hadley clockwise circulation (blue triangles in Fig. 7a) and to weaken the Southern Hemisphere counterclockwise circulation (purple triangles in Fig. 7a). While the magnitude of the change in the Hadley cell strength is similar in both the full nARF and nARF_1^0 simulations, the latter does not saturate at large amplitudes ($\alpha > 7 \text{ W m}^{-2}$). The ITCZ shifts southward (Fig. 7f), while the Hadley cells' descending branches show minor latitudinal shifts (Fig. 7b), as in the full nARF. Similar to the full nARF simulations, the precipitation intensity at the ITCZ decreases, in concert with the weakening of the Southern Hemisphere Hadley cell. This is similar to Kang et al. (2008), who showed that an asymmetrical extratropical heating results in a southward shift of the ITCZ and a decrease in precipitation

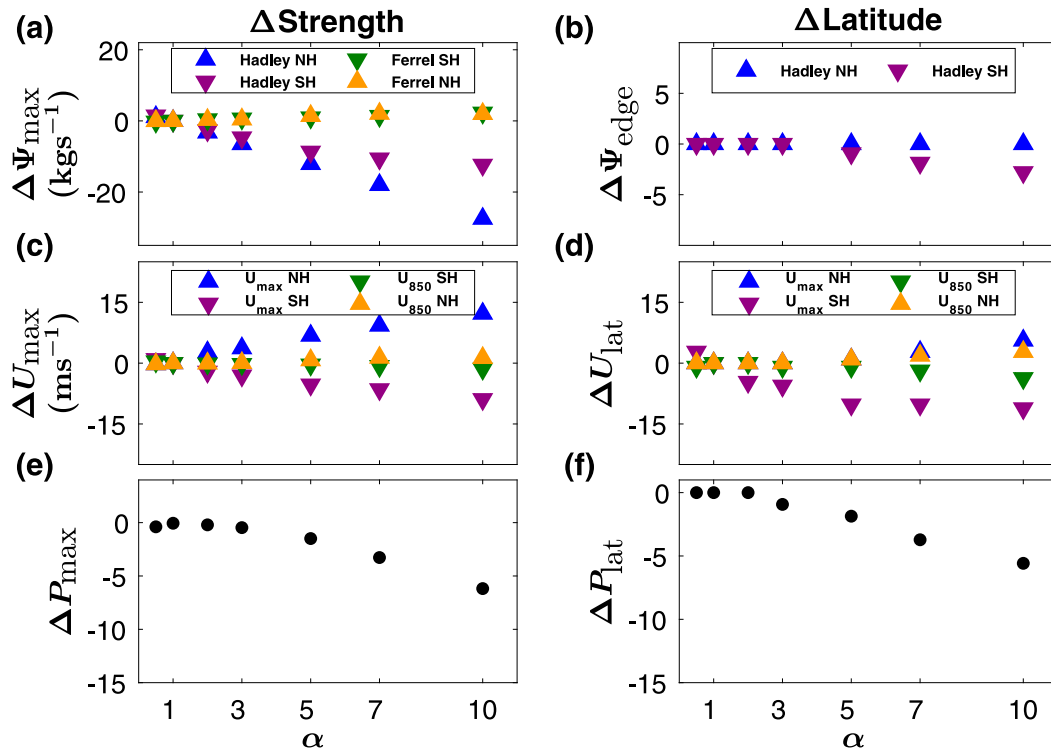


FIG. 7. The (a),(c),(e) strength and (b),(d),(f) latitudinal location of the mean fields from simulations forced by the first strongest mode of the nARF (nARF_1^0 ; Fig. 1b) relative to a simulation with $\alpha = 1 \text{ W m}^{-2}$, as a function of α , which controls the amplitude of the nARF. In (a)–(d) upward (downward) triangles represent Northern (Southern) Hemisphere values. The Hadley (blue and purple triangles) and Ferrel (orange and green triangles) cells strength ($10^{10} \text{ kg s}^{-1}$) are shown in (a). The Hadley cell edge (in latitude, defined where the meridional mass streamfunction first changes sign at the height of its max value) is shown in (b). The max zonal wind strength (blue and purple triangles) and zonal wind at 850 hPa (orange and green triangles) (m s^{-1}) are shown in (c). Latitude of max zonal wind (blue and purple triangles) and of eddy-driven jet (based on max zonal wind at 850 hPa, orange and green triangles) are shown in (d). (e),(f) Max precipitation intensity ($10^{-5} \text{ kg m}^{-2} \text{ s}^{-1}$) and latitude, respectively.

intensity as the heating difference between the two hemispheres increases.

As in the full nARF simulations, the southward shift of the ITCZ under nARF_1^0 results in a positive cross-equatorial energy flux, which increases with nARF_1^0 amplitude (black lines in Figs. 8a–c). The nARF_1^0 simulations produce similar changes in the behavior of both the tropical mean and eddy fields as in the full nARF simulations. The mean fields are responsible for most of the cross-equatorial energy flux (blue lines in Figs. 8a–c), and the eddy fields capture the acceleration of the superrotating jet at the equator by converging momentum there and diverging it around approximately 15°S (Fig. 8d). These changes in the eddy fields are likely to be related to the fact that the meridional gradient of potential vorticity changes sign around 15°S (mostly due to its barotropic component) as the ITCZ shifts southward (not shown). This satisfies the Rayleigh–Kuo criterion for barotropic instability (Kuo 1949) and thus modulates the eddy momentum flux behavior

around the equator (e.g., Williams 2003; Mitchell and Vallis 2010).

The nARF_1^0 simulations also captures the strengthening (weakening) of the Northern (Southern) Hemisphere mean zonal wind (blue and purple triangles in Fig. 7c) of the full nARF simulations. As discussed above, these changes in the winds are associated, through thermal wind balance, with changes in the meridional temperature gradient in these simulations. The nARF_1^0 acts to increase the meridional temperature gradient in the Northern Hemisphere and to weaken it in the Southern Hemisphere (Fig. 1b). The latter pushes the mean zonal wind poleward in the Southern Hemisphere as in the full nARF simulation (purple triangles in Fig. 7d).

The nARF_1^0 captures not only the tropical circulation's changes as in the full nARF simulations, but also the modulation of the Southern Hemisphere extratropical circulation. The nARF_1^0 acts to decrease the meridional temperature gradient in the Southern

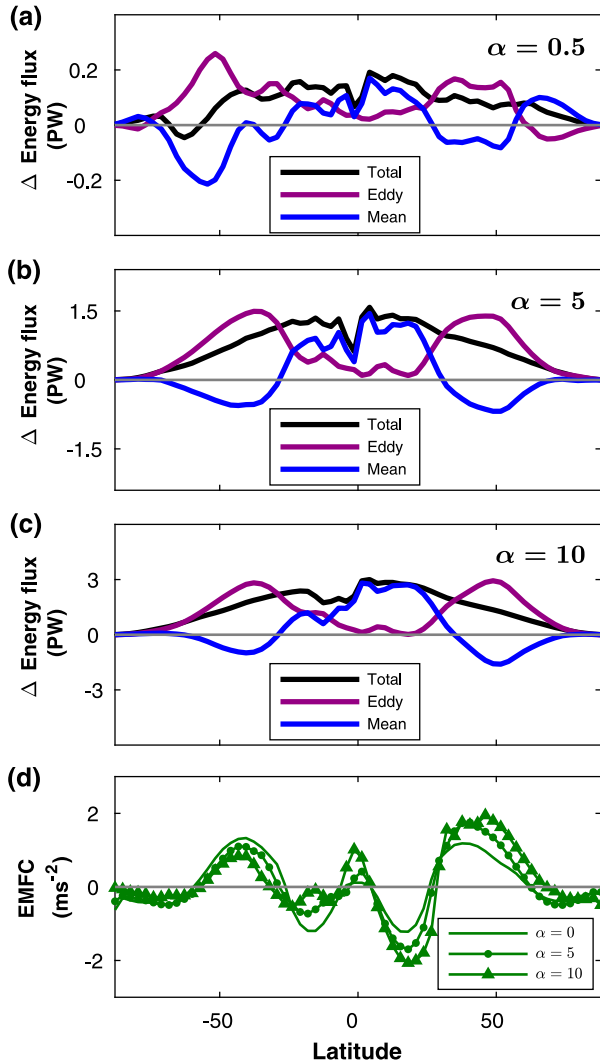


FIG. 8. Zonal and time mean eddy flow response to different amplitudes of the first strongest mode of the nARF (nARF_1^0 , Fig. 1b) as a function of latitude. Note the different y axes in all panels. (a)–(c) As in Fig. 3c, but showing the differences in vertically integrated mean moist static energy flux (PW) between simulations with ARF_1^0 using $\alpha = 0.5, 5$, and 10 W m^{-2} , respectively, and the reference simulation (Fig. 2). Black, blue, and purple lines correspond to meridional flux of total, mean, and eddy moist static energy, respectively. (d) Tropospheric vertically averaged mean EMFC [10^{-5} m s^{-2} ; the meridional component of the divergence of the EP flux, Eq. (3)] from the reference simulation (solid line), and simulations with nARF_1^0 using $\alpha = 5$ (circles) and 10 W m^{-2} (triangles).

Hemisphere, which weakens the eddy energy (purple lines in Figs. 8a–c) and momentum (green lines in Fig. 8d) transfers at midlatitudes. This results in a weaker meridional gradient of the eddy fluxes, in concert with weaker eddy-driven jet and Ferrel cell (green triangles in Figs. 7a and 7d). In the Northern Hemisphere, the nARF_1^0 captures part of the strengthening of the Ferrel

cell (orange triangles in Fig. 7a) and of the eddy-driven jet (orange triangles in Fig. 7d, and strengthening of the eddy momentum flux convergence in Fig. 8d). The nARF_1^0 captures only part of these changes of the mean fields in the extratropical Northern Hemisphere, as it fails to produce the weakening of the eddy fluxes in these latitudes, as in the full nARF simulations (purple lines in Figs. 8a–c). While the eddy fluxes in the full nARF simulations weaken at high latitudes, in the nARF_1^0 simulations they strengthen at midlatitudes. Both result in a strengthening of the meridional gradient of the eddy momentum and heat fluxes, and thus an increase in the mean fields. This, as further discussed below, indicates that the strengthening of the Northern Hemisphere meridional temperature gradient in the nARF_1^0 simulation is not the sole reason for the modulation of the mean and eddy fields in these latitudes.

b. ARF_4^0

The second most dominant mode (nARF_4^0 , which explains 10.3% of the variance) is also zonally symmetric (zonal wavenumber 0) but has total wave-number 4 (Fig. 1c). This forcing represents the cooling of mid-to-low latitudes in comparison to low and high latitudes (especially in the Northern Hemisphere). This mode does not capture the southward shift of tropical circulation in the full nARF simulations, as it lacks the meridional asymmetry around the equator. Thus, the Northern and Southern Hemisphere show similar behaviors. The ITCZ remains around the equator, as in the reference simulation (Fig. 9f), and the descending branches of the Hadley cell do not shift poleward (Fig. 9b). In addition, because the ITCZ does not shift off the equator, the cross-equatorial energy flux is zero (Figs. 10a–c). The cooling of midlatitudes relative to the tropics increases the meridional temperature gradient at the edge of the Hadley cell in both hemispheres, which increases the intensity of both the Hadley cell (Fig. 9a) and the ITCZ precipitation (Fig. 9e), but with a smaller magnitude than in the full nARF simulations (Fig. 4). Again, because of the lack of meridional asymmetry around the equator, this mode does not explain the tropical changes observed in the full nARF simulation.

In the extratropics, on the other hand, changes in the circulation are similar to the changes in the Northern Hemisphere full nARF simulations. The mean zonal wind increases (blue triangles in Fig. 9c), and its maximum slightly shifts poleward (3° latitude in comparison to 10° in the full nARF simulation, with an $\alpha = 10 \text{ W m}^{-2}$ scenario; blue triangles in Fig. 9d). This implies the importance of the increased meridional temperature

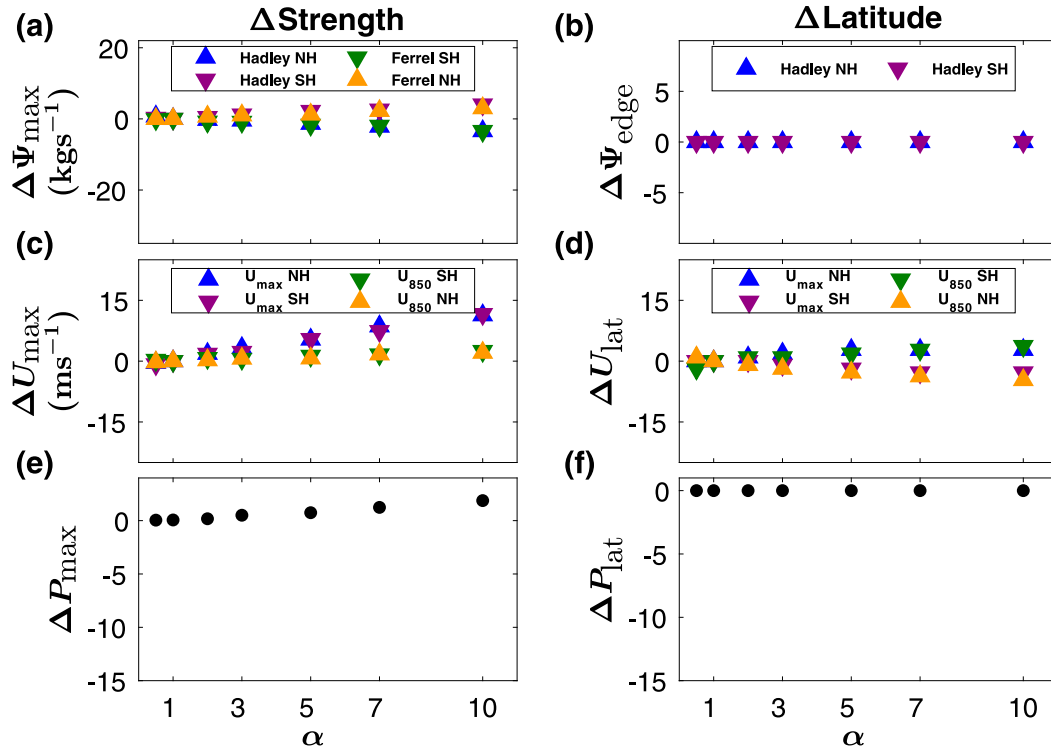


FIG. 9. The (a),(c),(e) strength and (b),(d),(f) latitudinal location of the mean fields from simulations forced by the second strongest mode of the nARF (nARF_4^0 , Fig. 1c) relative to a simulation with $\alpha = 1 \text{ W m}^{-2}$, as a function of α , which controls the amplitude of the nARF_4^0 . In (a)–(d) upward (downward) triangles represent Northern (Southern) Hemisphere values. The Hadley (blue and purple triangles) and Ferrel (orange and green triangles) cells strength ($10^{10} \text{ kg s}^{-1}$) are shown in (a). The Hadley cell edge (in latitude, defined where the meridional mass streamfunction first changes sign at the height of its max value) is shown in (b). The max zonal wind strength (blue and purple triangles) and zonal wind at 850 hPa (orange and green triangles) (m s^{-1}) are shown in (c). Latitude of max zonal wind (blue and purple triangles) and of eddy driven jet (based on max zonal wind at 850 hPa, orange and green triangles) are shown in (d). (e),(f) Max precipitation intensity ($10^{-5} \text{ kg m}^{-2} \text{ s}^{-1}$) and latitude, respectively.

gradient between the extratropics and tropics in modulating the subtropical mean fields of the Northern Hemisphere in the full nARF simulations. This is opposite of the results from Allen et al. (2012b), where a decrease in the meridional temperature gradient at high latitudes resulted in an equatorward shift of the jet. Whereas in Allen et al. (2012b) only a localized heating affects the jet shift, here a more complicated spatial structure is used to force the system. In addition, the Ferrel cell (orange triangles in Fig. 9a) and the low-level jet (orange triangles in Fig. 9d) also intensify with nARF amplitude, with similar amplitude to the full nARF simulation. In contrast to the poleward shift of the low-level jet in the nARF_1^0 simulations (orange and green triangles in Fig. 7d), here the jet shifts equatorward in both hemispheres (orange and green triangles in Fig. 9d), resulting in the overall similar position of the jet in the full nARF simulations (orange and green triangles in Fig. 4d). The eddy fields, which drive the Ferrel cell, show similar behavior to the full nARF simulations,

mostly at high latitudes, where the nARF_4^0 acts to decrease the meridional temperature gradient. The meridional eddy energy fluxes weaken at high latitudes and strengthen at mid-to-low latitudes (purple lines in Figs. 10a–c), similar to the Northern Hemisphere's eddy behavior in the full nARF simulation (purple line in Fig. 3c). This, together with the increase of the eddy momentum flux convergence (Fig. 10d), accompanies the strengthening of both the Ferrel cell and eddy-driven jet with nARF_4^0 .

5. The zonally asymmetric mode of the aerosols' radiative forcing

The zonally asymmetric mode (nARF_1^1 ; Fig. 1d), which is the third most dominant mode (explains 8.8% of the variance), mostly captures the cooling resulting from the ARF at eastern longitudes in the Northern Hemisphere, relative to western longitudes (Fig. 11a). Figure 11 shows the differences in the mean fields

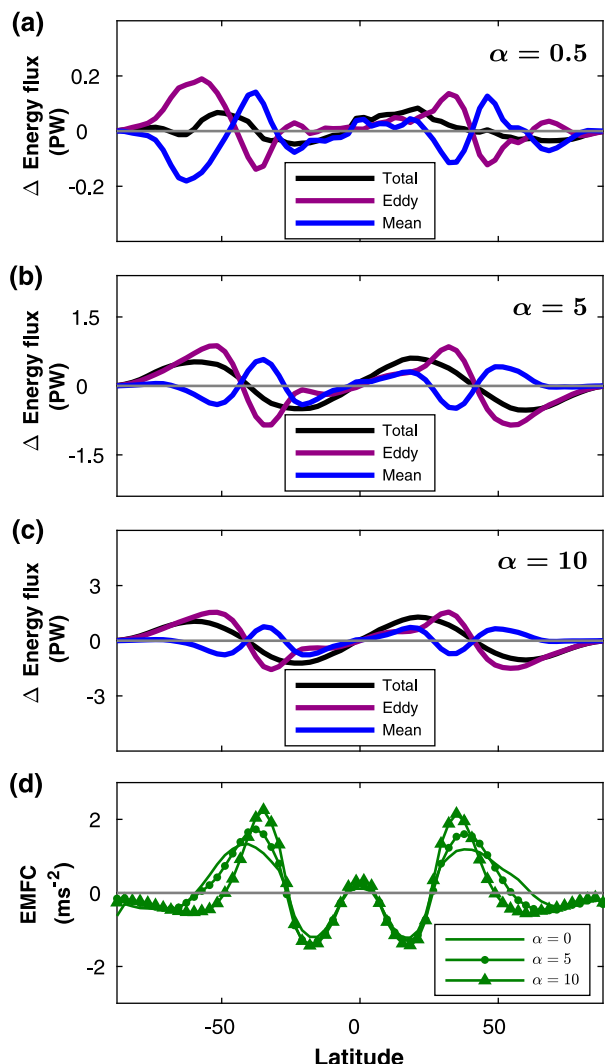


FIG. 10. Zonal and time mean eddy flow response to different amplitudes of the second strongest mode of the nARF (nARF_4^0 , Fig. 1c) as a function of latitude. Note the different y axes in all panels. (a)–(c) As in Fig. 3c, but showing the differences in vertically integrated mean moist static energy flux (PW) between simulations with ARF using $\alpha = 0.5, 5$, and 10 W m^{-2} , respectively, and the reference simulation (Fig. 2). Black, blue, and purple lines correspond to meridional flux of total, mean, and eddy moist static energy, respectively. (d) Tropospheric vertically averaged mean EMFC [10^{-5} m s^{-2} ; the meridional component of the divergence of the EP flux, Eq. (3)] from the reference simulation (solid line), and simulations with nARF_4^0 with $\alpha = 5$ (circles) and 10 W m^{-2} (triangles).

between the zonally asymmetric mode (nARF_1^1) simulation with $\alpha = 10 \text{ W m}^{-2}$ and the reference simulation as a function of latitude and longitude. As this mode is hemispherically symmetric, it does not capture the southward shift of the ITCZ (Figs. 3d and 6b,c), but rather in both hemispheres the tropical circulation strengthens in eastern longitudes (stronger ascending air

at the equator and descending air at the subtropics) and weakens in western longitudes (weaker ascending air at the equator and descending air at the subtropics) (Fig. 11b). Similar to the full nARF simulation, changes in zonal temperature gradients on eastern longitudes strengthen the poleward moving air at the upper branch of the Hadley cell, which strengthens the entire circulation at these longitudes. As in the full nARF simulation, this results in weaker precipitation rates at the subtropics (Fig. 11c).

Similar to the full nARF simulation (Fig. 6d), the zonally asymmetric mode also shows superrotating upper-level zonal wind at the equator (Fig. 11d). As was shown in two-layer models (e.g., Suarez and Duffy 1992; Saravanan 1993) and tidally locked idealized GCM (e.g., Merlis and Schneider 2010), zonally asymmetric tropical heating results in equatorial superrotation, because of the convergence of eddy momentum fluxes. Figure 12 shows the zonal spectrum of the eddy momentum flux convergence as a function of latitude, for three different forcing simulations (full nARF, nARF_1^0 , and nARF_1^1). The zonally asymmetric simulation (nARF_1^1) is forced by zonal wavenumber 1 (Fig. 1d), and the latter is mostly responsible for converging eddy momentum flux at the equator (red color at the equator in Fig. 12c) and diverging it at the subtropics (blue color in the subtropics in Fig. 12c). A similar picture occurs in the full nARF simulation (Fig. 12a), implying the importance of the cooling of eastern longitudes in the Northern Hemisphere in maintaining the equatorial superrotation. Although the nARF_1^0 has no zonal asymmetries, it also shows the importance of zonal wavenumber 1 in converging momentum at the equator, but with smaller amplitude (Fig. 12b). Including continents in these simulations might reduce the effect of zonal wavenumber 1 on the mean flow, because of the presence of stationary waves.

6. Summary

There is a large uncertainty regarding the magnitude of the global anthropogenic aerosol radiative forcing (ARF) (Alexander et al. 2013). The overall effect of anthropogenic aerosols on the temperature field may reduce the warming caused by greenhouse gases. Hence, it is crucial to better understand how aerosols may modulate the global-mean fields. However, even with zero global-mean ARF, the ARF's spatial distribution may still modulate the spatial distribution of the temperature field, which drives changes in the atmospheric circulation. In this study we show the importance of the spatial distribution of the direct anthropogenic ARF in modulating the atmospheric general circulation. Using

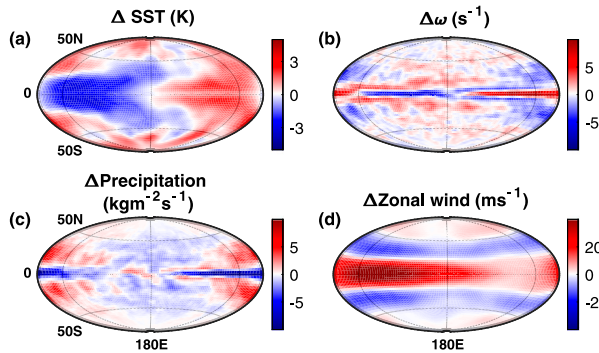


FIG. 11. Differences in time mean fields between simulation with the third strongest mode of the nARF (nARF_1^1 , Fig. 1d) with $\alpha = 10 \text{ W m}^{-2}$ and the reference simulation: (a) temperature (K), (b) vertical wind (10^{-7} s^{-1}) at the level of its max ITCZ value (780 hPa), (c) precipitation ($10^{-5} \text{ kg m}^{-2} \text{ s}^{-1}$), and (d) zonal wind (m s^{-1}) at the level of its max equatorial value (200 hPa).

an idealized GCM forced by an estimated direct anthropogenic shortwave ARF, from Copernicus Atmosphere Monitoring Service, the ARF's effect is studied by globally decomposing it and investigating the circulation's response to the most dominant modes under a range of different amplitudes. In spite of the relative simple approach taken here to represent the aerosol radiative forcing in an idealized GCM, the circulation's response to this forcing is similar to the findings of previous comprehensive GCM studies.

In the tropics, the ARF modulates the circulation mostly due to the higher concentration of aerosols in the Northern Hemisphere in comparison to the Southern Hemisphere. As the net radiative effect of aerosols is to cool the atmosphere, this meridional asymmetry, which is the most dominant mode of the ARF, acts to cool the Northern Hemisphere more than the Southern Hemisphere. As a result, the ITCZ shifts

southward (similar to Northern Hemisphere winter) while reducing its precipitation, in concert with the weakening of the Southern Hemisphere Hadley cell (the meridional temperature gradient decreases). The southward movement of the ITCZ results in a positive cross-equatorial moist energy flux, mostly due to the increase in the mean fields. On the other hand, the Northern Hemisphere Hadley cell strengthens as the meridional temperature gradient increases in the Northern Hemisphere. In both hemispheres, however, the edge of the Hadley cell shows minor latitudinal variations. In addition, the higher aerosol concentrations in Asia in comparison to North America results in a zonal wavenumber-1 forcing pattern in the Northern Hemisphere (third most dominant mode of the ARF). This zonal wavenumber is responsible for converging momentum at the equator, through eddy fluxes, which results in an equatorial superrotating jet.

In the Southern Hemisphere extratropics, the reduction in the meridional temperature gradient weakens the subtropical jet and pushes it poleward, further merging with the eddy-driven jet. Furthermore, this reduction also weakens the meridional eddy momentum and heat fluxes. Because the eddy-driven jet and Ferrel cell are driven by the eddy fluxes' meridional gradient, the latter's decrease at midlatitudes is in concert with the weakening of the extratropical mean fields in the Southern Hemisphere.

In the Northern Hemisphere, on the other hand, most of the ARF resides at midlatitudes, which increases the meridional temperature gradient between low and middle latitudes. This strengthens and pushes poleward the subtropical jet, which further merges with the eddy-driven jet (which shows minor latitudinal changes with ARF). The high aerosol concentration in the Northern

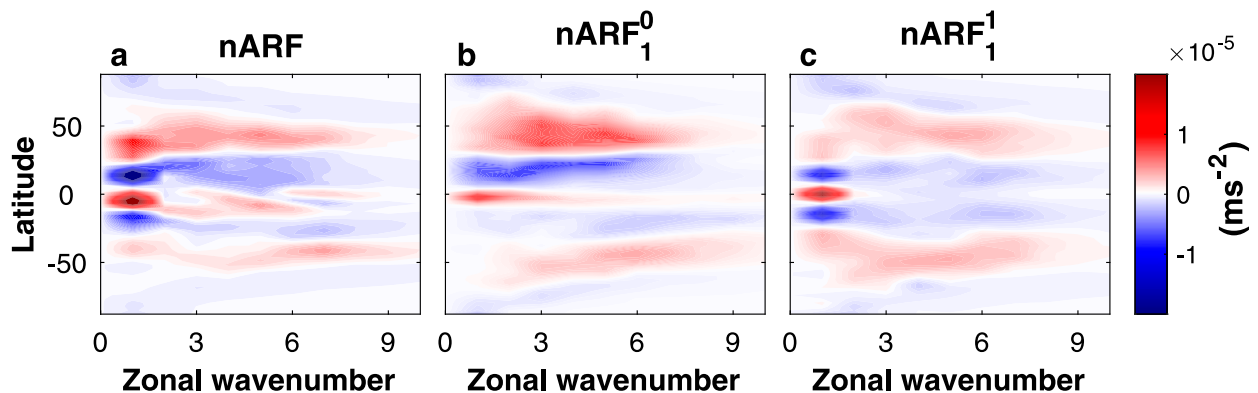


FIG. 12. EMFC spectra (10^{-5} m s^{-2}) as a function of latitude and zonal wavenumber for simulations with (a) full nARF (Fig. 1a), (b) the strongest mode of the nARF (nARF_1^0 ; Fig. 1b), and (c) the third strongest mode of the nARF (nARF_1^1 ; Fig. 1d). In all panels $\alpha = 10 \text{ W m}^{-2}$, and the spectra are calculated at the pressure of max EMFC of 230 hPa.

Hemisphere midlatitudes also reduces the temperature gradient between the middle and high latitudes, which is the second most dominant mode of the ARF. This reduces the meridional eddy momentum and heat fluxes at high latitudes, which is in concert with the strengthening of both the Ferrel cell and the eddy-driven jet in the Northern Hemisphere.

In the future, changes in the spatial distribution of aerosol's emissions may change the relative importance of the different modes of the ARF. Thus, the effects of the different modes on the general circulation, discussed here under different amplitudes, may help elucidate the future response of the general circulation to the projected aerosol forcing. For example, a decrease in aerosol emissions in Asia would decrease the zonal asymmetric effects of the ARF on the general circulation (e.g., would decrease the equatorial superrotation) and would reduce the effects of meridional asymmetry between the Northern and Southern Hemispheres (e.g., the southward shift and weakening of the ITCZ).

While the idealized GCM enables elucidating the effects of the spatial distribution of the ARF on the general circulation, it lacks several processes that may play an important role in a more realistic framework. For example, one feature that was found in previous studies using comprehensive GCM and does not appear in the above simulations is the contraction of the Hadley cell under aerosol forcing (Allen and Ajoku 2016). As the Hadley cell width is controlled by the vertical structure of temperature at the subtropics (Held 2000), the lack of a realistic radiation scheme, together with the simplified ARF vertical distribution (which was found to affect the width of the Hadley circulation; Kim et al. 2015), may explain this discrepancy. Another example is the idealized lower boundary in these simulations. The lack of continents omits the effect of stationary waves, and thus the importance of the zonal asymmetric mode in driving the superrotating jet at the equator may be overestimated.

Acknowledgments. We thank Ilan Koren and Yohai Kaspi for very fruitful discussions during the preparation of this paper and for supporting this manuscript. This research has been supported by the Israeli Science Foundation (Grant 1819/16 to Yohai Kaspi) and the Lev-Zion scholarship.

REFERENCES

- Albrecht, B. A., 1989: Aerosols, cloud microphysics, and fractional cloudiness. *Science*, **245**, 1227–1230, <https://doi.org/10.1126/science.245.4923.1227>.
- Alexander, L. V., and Coauthors, 2013: Summary of policymakers. *Climate Change 2013: The Physical Basis*, T. F. Stocker et al., Eds., Cambridge University Press, 3–29.
- Allen, R. J., 2015: A 21st century northward tropical precipitation shift caused by future anthropogenic aerosol reductions. *J. Geophys. Res.*, **120**, 9087–9102, <https://doi.org/10.1002/2015JD023623>.
- , and S. C. Sherwood, 2011: The impact of natural versus anthropogenic aerosols on atmospheric circulation in the Community Atmosphere Model. *Climate Dyn.*, **36**, 1959–1978, <https://doi.org/10.1007/s00382-010-0898-8>.
- , and O. Ajoku, 2016: Future aerosol reductions and widening of the northern tropical belt. *J. Geophys. Res.*, **121**, 6765–6786, <https://doi.org/10.1002/2016JD024803>.
- , S. C. Sherwood, J. R. Norris, and C. S. Zender, 2012a: Recent Northern Hemisphere tropical expansion primarily driven by black carbon and tropospheric ozone. *Nature*, **485**, 350–354, <https://doi.org/10.1038/nature11097>.
- , —, —, and —, 2012b: The equilibrium response to idealized thermal forcings in a comprehensive GCM: Implications for recent tropical expansion. *Atmos. Chem. Phys.*, **12**, 4795–4816, <https://doi.org/10.5194/acp-12-4795-2012>.
- , A. T. Evan, and B. B. B. Booth, 2015: Interhemispheric aerosol radiative forcing and tropical precipitation shifts during the late twentieth century. *J. Climate*, **28**, 8219–8246, <https://doi.org/10.1175/JCLI-D-15-0148.1>.
- Ban-Weiss, G. A., L. Cao, G. Bala, and K. Caldeira, 2012: Dependence of climate forcing and response on the altitude of black carbon aerosols. *Climate Dyn.*, **38**, 897–911, <https://doi.org/10.1007/s00382-011-1052-y>.
- Bellouin, N., J. Quaas, J.-J. Morcrette, and O. Boucher, 2013: Estimates of aerosol radiative forcing from the MACC reanalysis. *Atmos. Chem. Phys.*, **13**, 2045–2062, <https://doi.org/10.5194/acp-13-2045-2013>.
- Betts, A. K., 1986: A new convective adjustment scheme. Part I: Observational and theoretical basis. *Quart. J. Roy. Meteor. Soc.*, **112**, 677–691, <https://doi.org/10.1002/qj.49711247307>.
- , and M. J. Miller, 1986: A new convective adjustment scheme. Part II: Single column tests using GATE wave, BOMEX, ATEX and Arctic air-mass data sets. *Quart. J. Roy. Meteor. Soc.*, **112**, 693–709, <https://doi.org/10.1002/qj.49711247308>.
- Broccoli, A. J., K. A. Dahl, and R. J. Stouffer, 2006: Response of the ITCZ to Northern Hemisphere cooling. *Geophys. Res. Lett.*, **33**, L01702, <https://doi.org/10.1029/2005GL024546>.
- Ceppi, P., Y.-T. Hwang, X. Liu, D. M. W. Frierson, and D. L. Hartmann, 2013: The relationship between the ITCZ and the Southern Hemispheric eddy-driven jet. *J. Geophys. Res.*, **118**, 5136–5146, <https://doi.org/10.1002/jgrd.50461>.
- Chemke, R., 2017: Atmospheric energy transfer response to global warming. *Quart. J. Roy. Meteor. Soc.*, **143**, 2296–2308, <https://doi.org/10.1002/qj.3086>.
- Chung, E.-S., and B. J. Soden, 2017: Hemispheric climate shifts driven by anthropogenic aerosol–cloud interactions. *Nat. Geosci.*, **10**, 566–571, <https://doi.org/10.1038/ngeo2988>.
- Chung, S. H., and J. H. Seinfeld, 2005: Climate response of direct radiative forcing of anthropogenic black carbon. *J. Geophys. Res.*, **110**, D11102, <https://doi.org/10.1029/2004JD005441>.
- Dagan, G., and R. Chemke, 2016: The effect of subtropical aerosol loading on equatorial precipitation. *Geophys. Res. Lett.*, **43**, 11 048–11 056, <https://doi.org/10.1002/2016GL071206>.
- , I. Koren, O. Altaratz, and R. H. Heiblum, 2016: Aerosol effect on the evolution of the thermodynamic properties

- of warm convective cloud fields. *Sci. Rep.*, **6**, 38769, <https://doi.org/10.1038/srep38769>.
- , —, —, and —, 2017: Time-dependent, non-monotonic response of warm convective cloud fields to changes in aerosol loading. *Atmos. Chem. Phys.*, **17**, 7435–7444, <https://doi.org/10.5194/acp-17-7435-2017>.
- Eady, E. T., 1949: Long waves and cyclone waves. *Tellus*, **1** (3), 33–52, <https://doi.org/10.3402/tellusa.v1i3.8507>.
- Edmon, J. H. J., B. J. Hoskins, and M. E. McIntyre, 1980: Eliassen–Palm cross sections for the troposphere. *J. Atmos. Sci.*, **37**, 2600–2616, [https://doi.org/10.1175/1520-0469\(1980\)037<2600:EPCSFT>2.0.CO;2](https://doi.org/10.1175/1520-0469(1980)037<2600:EPCSFT>2.0.CO;2).
- Frierson, D. M. W., and Y.-T. Hwang, 2012: Extratropical influence on ITCZ shifts in slab ocean simulations of global warming. *J. Climate*, **25**, 720–733, <https://doi.org/10.1175/JCLI-D-11-00116.1>.
- , I. M. Held, and P. Zurita-Gotor, 2006: A gray-radiation aquaplanet moist GCM. Part I: Static stability and eddy scale. *J. Atmos. Sci.*, **63**, 2548–2566, <https://doi.org/10.1175/JAS3753.1>.
- Goody, R. M., and Y. L. Yung, 1995: *Atmospheric Radiation: Theoretical Basis*. 2nd ed. Oxford University Press, 519 pp.
- Haywood, J. M., A. Jones, N. Bellouin, and D. Stephenson, 2013: Asymmetric forcing from stratospheric aerosols impacts Sahelian rainfall. *Nature Climate Change*, **3**, 660–665, <https://doi.org/10.1038/nclimate1857>.
- Held, I. M., 2000: The general circulation of the atmosphere. Program in Geophysical Fluid Dynamics, Woods Hole Oceanographic Institution, 70 pp., https://www.gfdl.noaa.gov/wp-content/uploads/files/user_files/ih/lectures/woods_hole.pdf.
- , and A. Y. Hou, 1980: Nonlinear axially symmetric circulations in a nearly inviscid atmosphere. *J. Atmos. Sci.*, **37**, 515–533, [https://doi.org/10.1175/1520-0469\(1980\)037<0515:NASCIA>2.0.CO;2](https://doi.org/10.1175/1520-0469(1980)037<0515:NASCIA>2.0.CO;2).
- , and B. J. Soden, 2006: Robust responses of the hydrological cycle to global warming. *J. Climate*, **19**, 5686–5699, <https://doi.org/10.1175/JCLI3990.1>.
- Hwang, Y. T., D. M. W. Frierson, and S. M. Kang, 2013: Anthropogenic sulfate aerosol and the southward shift of tropical precipitation in the late 20th century. *Geophys. Res. Lett.*, **40**, 2845–2850, <https://doi.org/10.1002/grl.50502>.
- Inness, A., and Coauthors, 2013: The MACC reanalysis: An 8 yr data set of atmospheric composition. *Atmos. Chem. Phys.*, **13**, 4073–4109, <https://doi.org/10.5194/acp-13-4073-2013>.
- Kang, S. M., I. M. Held, D. M. W. Frierson, and M. Zhao, 2008: The response of the ITCZ to extratropical thermal forcing: Idealized slab-ocean experiments with a GCM. *J. Climate*, **21**, 3521–3532, <https://doi.org/10.1175/2007JCLI2146.1>.
- Key, J. R., and A. J. Schweiger, 1998: Tools for atmospheric radiative transfer: Streamer and FluxNet. *Comput. Geosci.*, **24**, 443–451, [https://doi.org/10.1016/S0098-3004\(97\)00130-1](https://doi.org/10.1016/S0098-3004(97)00130-1).
- Kim, H., S. M. Kang, Y.-T. Hwang, and Y.-M. Yang, 2015: Sensitivity of the climate response to the altitude of black carbon in the northern subtropics in an aquaplanet GCM. *J. Climate*, **28**, 6351–6359, <https://doi.org/10.1175/JCLI-D-15-0037.1>.
- Kinne, S., and Coauthors, 2013: MAC-v1: A new global aerosol climatology for climate studies. *J. Adv. Model. Earth Syst.*, **5**, 704–740, <https://doi.org/10.1002/jame.20035>.
- Kuo, H., 1949: Dynamic instability of two-dimensional non-divergent flow in a barotropic atmosphere. *J. Meteor.*, **6**, 105–122, [https://doi.org/10.1175/1520-0469\(1949\)006<0105:DIOTDN>2.0.CO;2](https://doi.org/10.1175/1520-0469(1949)006<0105:DIOTDN>2.0.CO;2).
- Lindzen, R. S., and A. V. Hou, 1988: Hadley circulations for zonally averaged heating centered off the equator. *J. Atmos. Sci.*, **45**, 2416–2427, [https://doi.org/10.1175/1520-0469\(1988\)045<2416:HCFZAH>2.0.CO;2](https://doi.org/10.1175/1520-0469(1988)045<2416:HCFZAH>2.0.CO;2).
- Merlis, T. M., and T. Schneider, 2010: Atmospheric dynamics of Earth-like tidally locked aquaplanets. *J. Adv. Model. Earth Syst.*, **2** (13), <https://doi.org/10.3894/JAMES.2010.2.13>.
- Ming, Y., and V. Ramaswamy, 2009: Nonlinear climate and hydrological responses to aerosol effects. *J. Climate*, **22**, 1329–1339, <https://doi.org/10.1175/2008JCLI2362.1>.
- , and —, 2011: A model investigation of aerosol-induced changes in tropical circulation. *J. Climate*, **24**, 5125–5133, <https://doi.org/10.1175/2011JCLI4108.1>.
- , —, and G. Chen, 2011: A model investigation of aerosol-induced changes in boreal winter extratropical circulation. *J. Climate*, **24**, 6077–6091, <https://doi.org/10.1175/2011JCLI4111.1>.
- Mitchell, J. L., and G. K. Vallis, 2010: The transition to superrotation in terrestrial atmospheres. *J. Geophys. Res.*, **115**, E12008, <https://doi.org/10.1029/2010JE003587>.
- Mlawer, E. J., S. J. Taubman, P. D. Brown, M. J. Iacono, and S. A. Clough, 1997: Radiative transfer for inhomogeneous atmospheres: RRTM, a validated correlated-k model for the longwave. *J. Geophys. Res.*, **102**, 16 663–16 682, <https://doi.org/10.1029/97JD00237>.
- Pedlosky, J., 1987: *Geophysical Fluid Dynamics*. 2nd ed. Springer-Verlag, 710 pp.
- Ramanathan, V., P. J. Crutzen, J. T. Kiehl, and D. Rosenfeld, 2001: Aerosols, climate, and the hydrological cycle. *Science*, **294**, 2119–2124, <https://doi.org/10.1126/science.1064034>.
- Ramaswamy, V., and C.-T. Chen, 1997: Linear additivity of climate response for combined albedo and greenhouse perturbations. *Geophys. Res. Lett.*, **24**, 567–570, <https://doi.org/10.1029/97GL00248>.
- Ridley, H. E., and Coauthors, 2015: Aerosol forcing of the position of the intertropical convergence zone since AD 1550. *Nat. Geosci.*, **8**, 195–200, <https://doi.org/10.1038/ngeo2353>.
- Roberts, D. L., and A. Jones, 2004: Climate sensitivity to black carbon aerosol from fossil fuel combustion. *J. Geophys. Res.*, **109**, D16202, <https://doi.org/10.1029/2004JD004676>.
- Robock, A., 2000: Volcanic eruptions and climate. *Rev. Geophys.*, **38**, 191–219, <https://doi.org/10.1029/1998RG000054>.
- Rotstayn, L. D., and U. Lohmann, 2002: Tropical rainfall trends and the indirect aerosol effect. *J. Climate*, **15**, 2103–2116, [https://doi.org/10.1175/1520-0442\(2002\)015<2103:TRTATI>2.0.CO;2](https://doi.org/10.1175/1520-0442(2002)015<2103:TRTATI>2.0.CO;2).
- , B. F. Ryan, and J. E. Penner, 2000: Precipitation changes in a GCM resulting from the indirect effects of anthropogenic aerosols. *Geophys. Res. Lett.*, **27**, 3045–3048, <https://doi.org/10.1029/2000GL011737>.
- Saravanan, R., 1993: Equatorial superrotation and maintenance of the general circulation in two-level models. *J. Atmos. Sci.*, **50**, 1211–1227, [https://doi.org/10.1175/1520-0469\(1993\)050<1211:ESAMOT>2.0.CO;2](https://doi.org/10.1175/1520-0469(1993)050<1211:ESAMOT>2.0.CO;2).
- Shindell, D. T., G. A. Schmidt, M. E. Mann, and G. Faluvegi, 2004: Dynamic winter climate response to large tropical volcanic eruptions since 1600. *J. Geophys. Res.*, **109**, D05104, <https://doi.org/10.1029/2003JD004151>.
- Stevens, B., and Coauthors, 2013: Atmospheric component of the MPI-M Earth system model: ECHAM6. *J. Adv. Model. Earth Syst.*, **5**, 146–172, <https://doi.org/10.1002/jame.20015>.
- Suarez, M. J., and D. G. Duffy, 1992: Terrestrial superrotation: A bifurcation of the general circulation. *J. Atmos. Sci.*, **49**,

- 1541–1554, [https://doi.org/10.1175/1520-0469\(1992\)049<1541:TSABOT>2.0.CO;2](https://doi.org/10.1175/1520-0469(1992)049<1541:TSABOT>2.0.CO;2).
- Twomey, S., 1977: The influence of pollution on the shortwave albedo of clouds. *J. Atmos. Sci.*, **34**, 1149–1152, [https://doi.org/10.1175/1520-0469\(1977\)034<1149:TIOPOT>2.0.CO;2](https://doi.org/10.1175/1520-0469(1977)034<1149:TIOPOT>2.0.CO;2).
- Vallis, G. K., 2006: *Atmospheric and Oceanic Fluid Dynamics*. Cambridge University Press, 770 pp.
- , P. Zurita-Gotor, C. Cairns, and J. Kidston, 2015: Response of the large-scale structure of the atmosphere to global warming. *Quart. J. Roy. Meteor. Soc.*, **141**, 1479–1501, <https://doi.org/10.1002/qj.2456>.
- Voigt, A., and Coauthors, 2017: Fast and slow shifts of the zonal-mean intertropical convergence zone in response to an idealized anthropogenic aerosol. *J. Adv. Model. Earth Syst.*, **9**, 870–892, <https://doi.org/10.1002/2016MS000902>.
- Wang, C., 2004: A modeling study on the climate impacts of black carbon aerosols. *J. Geophys. Res.*, **109**, D03106, <https://doi.org/10.1029/2003JD004084>.
- , 2007: Impact of direct radiative forcing of black carbon aerosols on tropical convective precipitation. *Geophys. Res. Lett.*, **34**, L05709, <https://doi.org/10.1029/2006GL028416>.
- , 2015: Anthropogenic aerosols and the distribution of past large-scale precipitation change. *Geophys. Res. Lett.*, **42**, 10 876–10 884, <https://doi.org/10.1002/2015GL066416>.
- Williams, G. P., 2003: Barotropic instability and equatorial super-rotation. *J. Atmos. Sci.*, **60**, 2136–2152, [https://doi.org/10.1175/1520-0469\(2003\)060<2136:BIAES>2.0.CO;2](https://doi.org/10.1175/1520-0469(2003)060<2136:BIAES>2.0.CO;2).
- Williams, K. D., A. Jones, D. L. Roberts, C. A. Senior, and M. J. Woodage, 2001: The response of the climate system to the indirect effects of anthropogenic sulfate aerosol. *Climate Dyn.*, **17**, 845–856, <https://doi.org/10.1007/s003820100150>.
- Yoshimori, M., and A. J. Broccoli, 2008: Equilibrium response of an atmosphere–mixed layer ocean model to different radiative forcing agents: Global and zonal mean response. *J. Climate*, **21**, 4399–4423, <https://doi.org/10.1175/2008JCLI2172.1>.